Separated electrodes for the enhancement of high-speed data transmission in vertical-cavity surface-emitting laser arrays

YAUNG-CHENG ZHAO,[1] ZOHAUDDIN AHMAD,[1] WU-MIN LONG,[1] ZUHAIB KHAN,[1] N. LEDENTSOV JR.,[2] ID **MARWAN BOU SANAYEH,[2] TE-LIEH PAN,[3] CHENG-CHUN CHEN,[4] CHIA-JUI CHANG,[4] TIEN-CHANG LU,[4]** ID **N. N. LEDENTSOV,[2] AND JIN-WEI SHI[1],***

[1]*Department of Electrical Engineering, National Central University, Jungli 320, Taiwan*
[2]*VI Systems GmbH, Hardenbergstr. 7, 10623 Berlin, Germany*
[3]*AboCom Systems, Inc., 2F, No. 50-8, Keyan Rd., Zhunan Township, Miaoli County, Taiwan*
[4]*Department of Photonics and Institute of Electro-Optical Engineering, College of Electrical and Computer Engineering, National Yang Ming Chiao Tung University, Hsinchu 30050, Taiwan*
*jwshi@ee.ncu.edu.tw

Abstract: In this work, a novel design for the electrodes in a near quasi-single-mode (QSM) vertical-cavity surface-emitting laser (VCSEL) array with Zn-diffusion apertures inside is demonstrated to produce an effective improvement in the high-speed data transmission performance. By separating the electrodes in a compact 2×2 coupled VCSEL array into two parts, one for pure dc current injection and the other for large ac signal modulation, a significant enhancement in the high-speed data transmission performance can be observed. Compared with the single electrode reference, which parallels 4 VCSEL units in the array, the demonstrated array with its separated electrode design exhibits greater dampening of electrical-optical (E-O) frequency response and a larger 3-dB E-O bandwidth (19 vs. 15 GHz) under the same amount of total bias current (20 mA). Moreover, this significant improvement in dynamic performance does not come at the cost of any degradation in the static performance in terms of the maximum near QSM optical output power (17 mW @ 20 mA) and the Gaussian-like optical far-field pattern which has a narrow divergence angle (full-width half maximum (FWHM): 10° at 20 mA). The advantages of the separated electrode design lead to a much better quality of 32 Gbit/sec eye-opening as compared to that of the reference device (jitter: 1.5 vs. 2.8 ps) and error-free 32 Gbit/sec transmissions over a 500 m multi-mode fiber has been achieved under a moderate total bias current of 20 mA.

1. Introduction

Vertical-cavity surface-emitting laser (VCSEL) arrays have plentiful applications nowadays, such as the light sources in optical wireless communication (OWC) channels [1–5], laser ranging and sensing [6–8], and in multi-core fiber communication channels [9–11]. In order to extend the ranging distance of a sensing system, minimize the diffraction loss in wireless communication channels or obtain good coupling efficiency between the VCSEL array and the fiber, it is highly desirable for the VCSEL array to produce single-mode (SM) and high brightness outputs [3,4,7]. One of the most straightforward ways to let the VCESL array be single-mode is by directly downscaling the oxide aperture diameter (< 3 μm) of the VCSEL. However, issues with the limited SM power and reliability due to high the operation current density impede the practical application of this VCSEL structure [11]. Devices having special cavity design [12] or extra optical apertures inside the VCSEL cavity, such as Zn-diffusion [13], surface-relief [14], or tunnel junction lithographic apertures [15], have been demonstrated to have high SM power with a reasonably low operation current density. Nevertheless, the spatial hole burning effect

[16–18] and dominant fundamental lasing mode in these high-power SM VCSELs can usually lead to undesired low-frequency roll-off in the electrical-to-optical (E-O) frequency response and peaking of the relative intensity noise (RIN) [4,16,17], respectively. These characteristics seriously degrade the large-signal transmission results [16]. In this work, we demonstrate a 2×2 near quasi-SM (QSM) VCSEL array with both a novel array layout and electrode design with a small pitch size (20 μm) between the light emission apertures, which can greatly enhance the high-speed transmission performance. In contrast to the traditional array with its single electrode to parallel 4 VCSEL units in the array, the demonstrated array has a dual electrode design, one for only dc current injection and the other for dc + radio-frequency (RF) signal modulation. According to the near-field measurement results, this non-uniform current injection from dual electrodes results in weak optical coupling between neighboring VCSEL units. In contrast to the results reported for devices with strongly coupled VCSEL cavities [19–21], which usually have significant bandwidth enhancement induced by strong resonance in their electrical-to-optical (E-O) frequency response, the weak coupling in our array leads to greater dampening of the electrical-optical (E-O) frequency response, a larger 3-dB E-O bandwidth (19 vs. 15 GHz), and much better quality of 32 Gbit/sec eye-opening than that of the reference device (jitter: 1.5 vs. 2.8 ps), under the same amount of total bias current (20 mA). Furthermore, excellent static performance in terms of high maximum near QSM optical output power (17 mW @ 20 mA) and Gaussian-like optical far-field patterns with a narrow divergence angle (full-width half maximum (FWHM): 10° at 20 mA) can be simultaneously achieved with this novel VCSEL array. The demonstrated VCSEL array structures show strong potential to greatly enhance the transmission performance in the next generation of optical wireless and data communication systems.

2. Design of device structure and fabrication

Figures 1(a) and (b) show top views of the demonstrated 2×2 array (device A) and reference one (device B), respectively. The insets show zoom-in views of their light emission regions. Figure 1(c) shows a conceptual 3-dimensional diagram of device A. Here, Zn-diffusion and oxide-relief apertures are adopted in our array to manipulate the number of optical modes in the output optical spectra and relax the RC-limited bandwidth, respectively [3]. The diameters of the Zn-diffusion (W_Z) and oxide-relief apertures (W_o) and the Zn-diffusion depths (d) of the measured devices are specified in Fig. 1(c) with the values appearing in the captions below each figure.

In the traditional VCSEL array, each VCSEL unit is usually an isolated pillar etched down to the substrate, paralleled by a common electrode on the topside of the chip. However, this type of layout makes optical phase couplings among neighboring VCSELs difficult due to the strong index contrast between the active mesa and the air, which results in strong evanescent wave loss. One of the most effective ways to enhance the phase coupling is by incorporating an optical waveguide between the different active mesas [22]. Here, the length of the connecting waveguide is set to be as short as possible, producing a dumbbell shaped active mesa. As specified in Fig. 1(a), the pitch size of the light emission aperture is 20 μm, which is too large to allow the phenomenon of strong cavity coupling. For this demonstrated array structure, we see evidence of coherence as a superstructure in the far-field patterns at pitch sizes of ∼12 μm and below [23]. A study of the influence of the different pitch sizes and different widths of connected regions between adjacent VCSELs on the static and dynamic performance will be included in future work. Although the mesa shape is not symmetrically circular, a near circular (square) wet oxidation aperture can still be obtained, as shown in the inset to Fig. 1(c). In contrast to device B, the topside of the mesa is covered by a single p-type electrode to parallel 4 VCSEL units; there are two separated p-type electrodes on the topside of device A. During high-speed operation, one side is for DC current while the other side is for DC + RF signal injection. We can thus expect the injection of DC light output from the neighboring two VCSEL units to the modulated
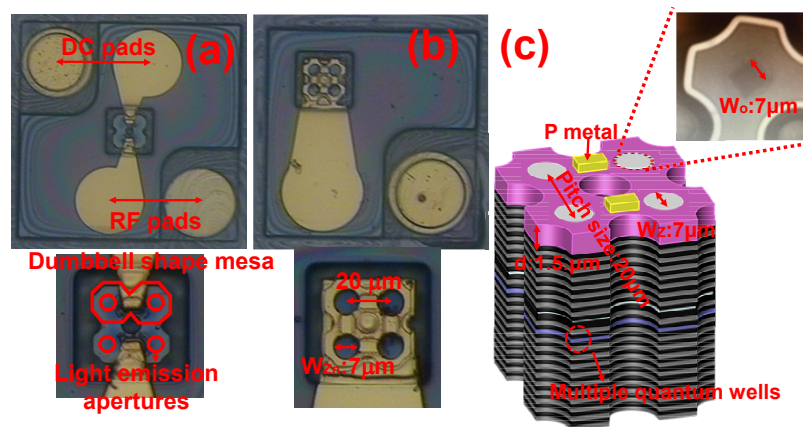
Fig. 1. Top view of the demonstrated 2×2 VCSEL array: (a) device A and (b) device B. The insets show zoom-in pictures of the active light emission apertures of two such devices. (c) Conceptual 3-dimensional diagram of active light-emission apertures in device A. An infrared photo of the aperture during the wet oxidation process is shown in the inset.

pair of VCSELs. This results in a significant improvement of dynamic performance which will be discussed latter. The VCSEL epi-layer structure is grown on a n^+ GaAs substrate, which is composed of four $In_{0.07}Ga_{0.9}As/Al_{0.3}Ga_{0.7}As$ (40/45 Å) MQWs sandwiched between 39-pair n-type and 24-pair p-type $Al_{0.93}Ga_{0.07}As/Al_{0.15}Ga_{0.85}As$ Distributed-Bragg-Reflector (DBR) layers with an $Al_{0.98}Ga_{0.02}As$ layer (25 nm thick) above the MQWs for oxidation [24]. Fabry-Perot (FP) dip mapping of the whole VCSEL wafer shows that the cavity resonant wavelength is located at around 850 nm and that detuning between the gain peak (838 nm) and FP dip (850 nm) wavelengths is at around 12 nm. Such detuning results in a significant improvement in the 3-dB O-E bandwidth of the VCSEL due to the device self-heating induced red-shift of the gain peak under high bias currents and high junction temperatures [25].

3. Measurement results

The free-space light output power versus current (L-I) characteristics of devices A and B and a comparison between their I-voltage (I-V) curves are shown in Figs. 2(a), (b), and (c), respectively. Here, a large area (1×1 cm^2) power sensor head is adopted to collect all of the output light from the 4 light emission apertures in our array. The two I-V curves shown in Fig. 2(c) for device A are measured separately from the DC and RF pads for a 1×2 VCSEL array. Note that their differential resistances are much larger than that of device B. This is because, in contrast to device B, which has a fully covered p-metal area outside the light emission aperture, the two electrodes in device A only partially cover this area, thus leading to a poorer I-V performance and more significant redshift in the optical spectra under high bias currents due to more serious ohmic heating. Nevertheless, due to the high resistivity of the p-DBR layers, this layout can provide some isolation between the two electrodes resulting in non-uniform current injection, which enhances the optical coupling between adjacent VCSEL units. This will be discussed in detail later based on the near-field measurement results for devices A and B. For the L-I measurement of device A, we sweep the injected DC bias current, as shown on the x-axis of Fig. 2(a), onto its RF electrode and then apply different DC bias currents to the DC electrodes, corresponding to the different L-I traces in this figure. We can clearly see that, as expected, the total output power from the array can be gradually increased by increasing the bias current on the two separated electrodes. As specified by the markers in Figs. 2(a) and (b), this dual electrode design can offer a

slight improvement in the output power (32.5 vs. 29.7 mW) under the same bias current (40 mA) compared to that of the traditional array with a single electrode. This may be attributed to the fact that the dual electrode design can minimize the current crowding and improve the current injection efficiency to our 2×2 array.
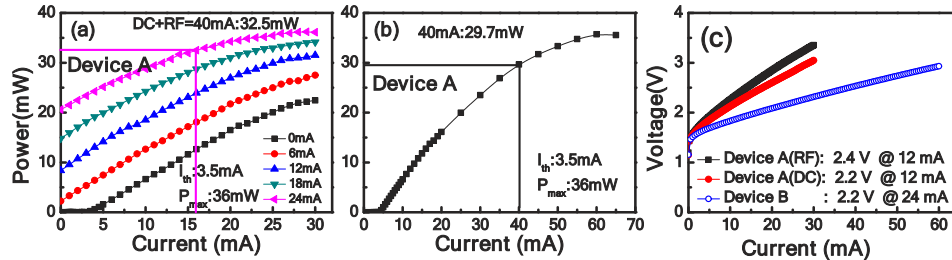
Fig. 2. Measured L-I curves of (a) device A and (b) device B. (c) Measured I-V curves of device A through the DC and RF pads and for B ($W_z/W_o/d = 7/7/1.5 \mu m$).

To ensure SM or QSM outputs from the VCSEL array, it is highly desirable to improve the coupling efficiency between the VCSEL array output and the fiber [3] and further extend its bandwidth-distance product through the multi-mode fiber (MMF) [17,26,27]. Figures 3(a), (b), and (c) show the measured bias dependent output optical spectra of device A with two different combinations of injected bias currents through the dual electrodes and device B, respectively. Here, each optical spectrum in Figs. 3(a) and (b) represent the spectra obtained with the injection of different bias currents to the RF electrodes; the injected bias currents to the DC electrodes are fixed at 6 and 8 mA, respectively. The maximum resolution of adopted optical spectrum analyzer (ANDO AQ6315A) is at around 0.05 nm. Thanks to the Zn-diffusion process, which can stabilize the output optical spectra, the QSM to near QSM output performance of both devices (A and B) is very similar, regardless of the change in combination of bias currents, and a near QSM output can be sustained from a low to high total bias current (~20 mA). To meet the requirements of perfect SM and QSM performance, the measured side-mode suppression ratio (SMSR) in optical spectra must be over 30 and 20 dB, respectively [17,26]. Here, under a 20 mA bias current, the corresponding SMSR (Figs. 3(a) to (c)) is around 2.5, 2.3, and 0.2 dB, respectively.
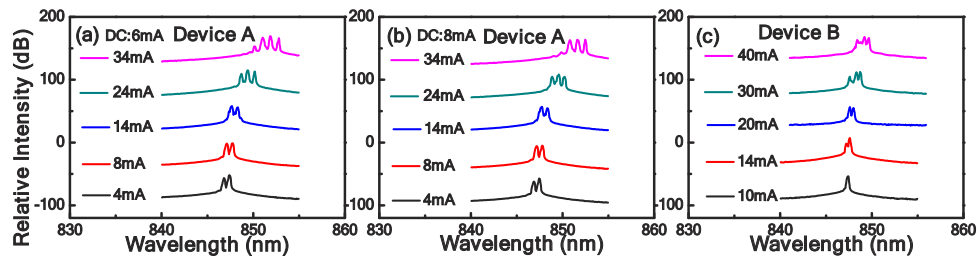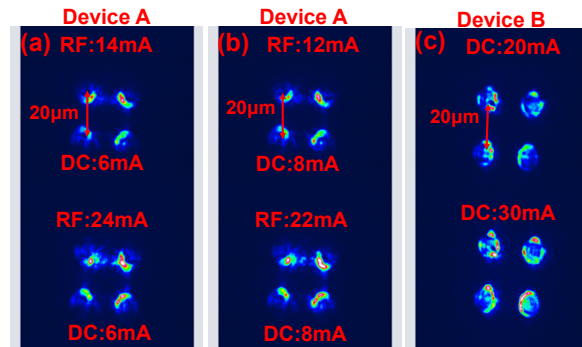

Fig. 3. Measured output optical spectra under different bias currents for (a) device A (dc electrode: 6 mA), (b) device A (dc electrode: 8 mA), and (c) device B ($W_z/W_o/d = 7/7/1.5 \mu m$).

Figures 4(a) to (c) show the corresponding bias dependent 1-dimensional (1-D) and 2-D far-field patterns (FFPs) of device A and device B, respectively, with two different combinations of bias current. It can be clearly seen that the narrow far-field divergence angle (full-width half maximum (FWHM): ~10° @ ~20 mA) and circular patterns of both devices are very similar under the same bias current. A slight broadening of the FFPs is mainly due to the rise of higher-order modes with the increase in the bias current, as shown by the measured bias dependent optical

spectra in Fig. 3. This measurement results confirm the good coupling efficiency between our demonstrated 2×2 array output and the OM4 MMF. The measured coupling efficiency obtained using the OM4 fiber with a lens fiber tip is at around 50%. In order to further improve this number and suppress the broadening of the measured FFPs, it is desirable to further increase the Zn-diffusion depth (d) or narrow the W_z to increase the intra-cavity loss, to obtain a perfect SM and bias invariant FFPs [17]. Figure 5 shows the near-field patterns (NFPs) for the same devices (A and B) measured under total bias currents of 20 and 30 mA and with two different bias currents (6 and 8 mA) to the DC pads. We can clearly see that, for device A, our dual electrode design with non-uniform current injection provides weak optical coupling between adjacent VCSEL units, leading to a significant improvement in its dynamic performance, which will be discussed in greater detail later.
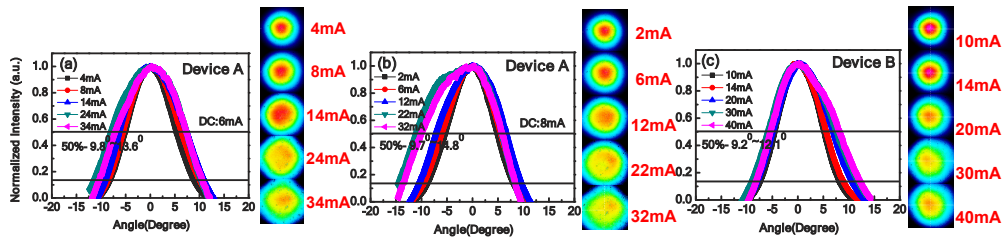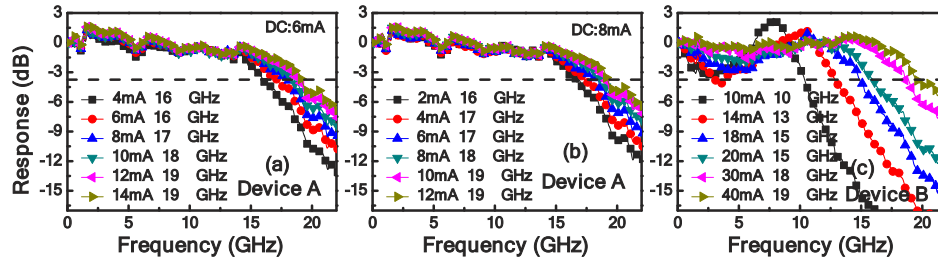

Fig. 4. Measured 1-D and 2-D far-field patterns under different bias currents for (a) device A (dc electrode: 6 mA), (b) device A (dc electrode: 8 mA), and (c) device B ($W_z/W_o/d = 7/7/1.5\,\mu m$).

Fig. 5. Measured 2-D near-field patterns under two different total bias currents as 20 and 30 mA for (a) device A (dc electrode: 6 mA), (b) device A (dc electrode: 8 mA), and (c) device B ($W_z/W_o/d = 7/7/1.5\,\mu m$).

The high-speed E-O performance of the fabricated devices was measured by a lightwave component analyzer (LCA), which was composed of a network analyzer (Anritsu 37397C) and a calibrated photoreceiver module (VI Systems: D50-850 M). Figures 6(a) and (b) show the measured bias dependent E-O frequency responses for device A with two different fixed currents (6 and 8 mA) to the DC electrodes. Figure 6(c) shows the measured bias dependent E-O frequency responses for device B. We can clearly see that, regardless of the combination of bias current, device A shows a wider 3-dB bandwidth than does device B (19 vs. 15 GHz) under the same total bias current. Furthermore, the E-O responses of device A are more flattened (dampened) than those of device B when the total bias current increases from 10 to 20 mA. As illustrated in Fig. 3, our device can sustain near QSM output under such a bias current regime (below 30 mA).

Both the flatter E-O responses and near QSM performance ensure the excellent transmission performance, which will be discussed in detail later. On the other hand, the E-O response of device B flattens when the bias current reaches 40 mA, however, this high bias current leads to multi-mode performance of the output optical spectra.


Fig. 6. Measured E-O frequency responses of (a) device A (dc electrode: 6 mA), (b) device A (dc electrode: 8 mA), and (c) device B under different bias currents ($W_z/W_o/d = 7/7/1.5\,\mu m$).

Figures 7(a) and (b) show the back-to-back (BTB) 32 Gbit/sec transmission results for devices A and B, respectively. During the transmission experiment, a high-speed photoreceiver module (RXM25DF; Thorlabs, Inc), comprised of a GaAs based p-i-n photodiode and a linear amplifier with a 25 GHz 3-dB optical-to-electrical bandwidth for the whole module, is used. A 32 Gbit/s non-return-to-zero (NRZ) electrical signal with a pseudo-random binary sequence (PRBS) length of 2^{15}-1 is generated through a pattern generator. The quality of the eye patterns of all tested devices was evaluated under optimized peak-to-peak driving voltages (V_{pp}) and bias currents. The optimized V_{pp} values of devices A and B are very close, ranging from 0.35 to 0.5 V. The close values of V_{pp} are mainly due to the quite similar frequency responses of the microwave reflection coefficients (S_{11}) during E-O response measurement (S_{21}) exhibited by these two devices. The values of the timing jitter in each eye pattern, which have clear eye-opening performance, are specified. As can be seen, device A shows much better eye-opening than that of device B under a bias current of 30 mA. Figure 8 shows the 32 Gbit/sec transmission results through a 500-meter OM5 fiber (CORNING; MM PATCHCORD OM5) for device A, with different combinations of total bias currents at 20 mA through dual electrodes. Error-free, clear eye-opening can be achieved thanks to the dampened E-O response and near QSM performance, as discussed above. In contrast to device A, device B does not achieve the same eye-opening performance under the same test conditions, due to the significant resonance in its E-O responses under moderate bias current (< 20 mA) for QSM performance.
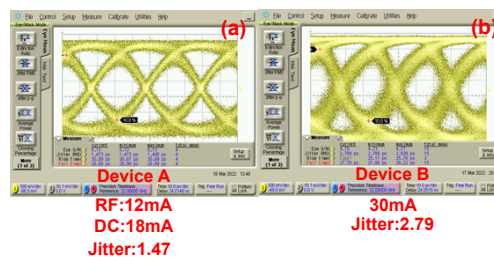

Fig. 7. Measured BTB 32 Gbit/sec transmission results using (a) device A and (b) device B ($W_z/W_o/d = 7/7/1.5\,\mu m$).

The superior dynamic performance of device A compared to device B can be attributed to that fact that the when the 2 VCSEL units in device A are under high-speed modulation, the photon density inside their cavities can be effectively increased due to the injection of constant
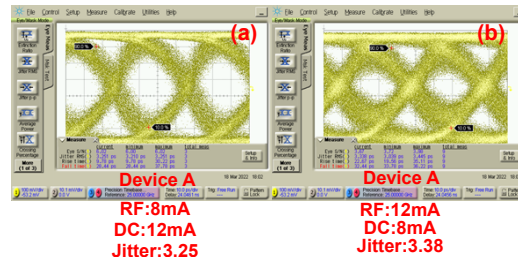
Fig. 8. Measured 32 Gbit/sec transmission results through a 500-meter OM5 fiber using device A with (a) (RF: 8 mA; dc: 12 mA) and (b) (RF: 12 mA; dc: 8 mA). ($W_z/W_o/d = 7/7/1.5 \, \mu m$).

optical power from 2 neighboring VCSEL units under a dc bias current. This is supported by the NFP measurement results shown in Fig. 5. The increase of photon density in the VCSEL cavity represents the suppression of the RIN level [28], which leads to the dampened of E-O frequency response and improved quality of eye patterns [4]. In contrast to device A, in device B, the injected AC driving current is shared equally between all of the four VCSEL units for modulation and as shown in Fig. 5(c), such uniform current injection weakens the optical coupling between neighboring VCSEL units. Except for external light injection to increase the photon density inside VCSEL cavity, the other straightforward way to increase photon density is to downscale the size of the oxide apertures. Figures 9–12 show the measured L-I-V, output optical spectra, 1-D/2-D far-field patterns, and 2-D near field patterns of device A and B but with smaller W_0 (4 vs. 7 μm), respectively.
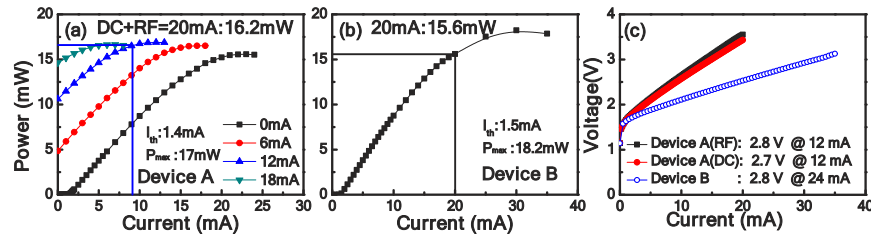

Fig. 9. Measured L-I curves of (a) device A and (b) device B. (c) Measured I-V curves of devices A and B ($W_z/W_o/d = 7/4/1.5 \, \mu m$).

We can clearly see that these results are very similar to the case where W_o is 7 μm, as illustrated in Figs. 2 to 5. Device A may produce a slightly larger output power (16.2 vs. 15.6 mW) than that of device B under the same bias current (20 mA) but both devices can sustain near QSM performance when the total bias current is less than 30 mA. The corresponding SMSRs under a bias current of 20 mA (as shown in Figs. 10(a) to (c)) are around 8.4, 9.5, and 4.5 dB, respectively. However, as can be seen in the measured NFPs in Fig. 12, there is no obvious optical coupling between adjacent VCSEL units in either device A or B. This can be attributed to the reduction in the number of optical transverse modes in the VCSEL cavities with the decrease of W_o, which results in a narrowing of the Gaussian-like NFPs so the coupling between neighboring VCSEL thus becomes less.

Figures 13–15 show the measured E-O frequency responses, 32 Gbit/sec eye patterns for BTB and 500-meter OM5 fiber transmission of these two devices (A and B), respectively. Compared with the measured E-O responses of device B with a larger W_o (7 μm), as shown in Fig. 6, we can clearly see that these responses can be effectively flattened when the W_o is downscaled from 7 to 4 μm due to the increase of photon density. Nevertheless, as shown in Figs. 13(a) and
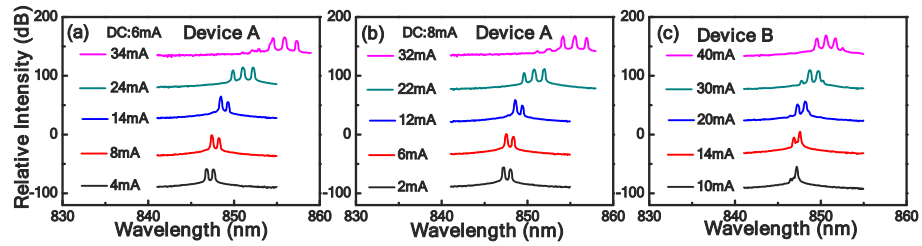
Fig. 10. Measured output optical spectra under different bias currents for (a) device A (dc electrode: 6 mA), (b) device A (dc electrode: 8 mA), and (c) device B ($W_z/W_o/d = 7/4/1.5$ μm).
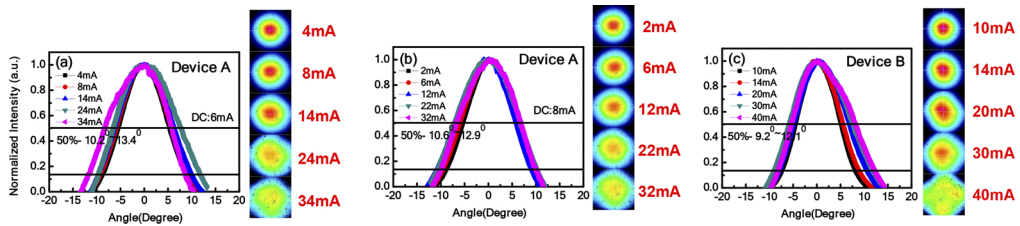
Fig. 11. Measured 1-D and 2-D far-field patterns under different bias currents for (a) device A (dc electrode: 6 mA), (b) device A (dc electrode: 8 mA), and (c) device B ($W_z/W_o/d = 7/4/1.5$ μm).
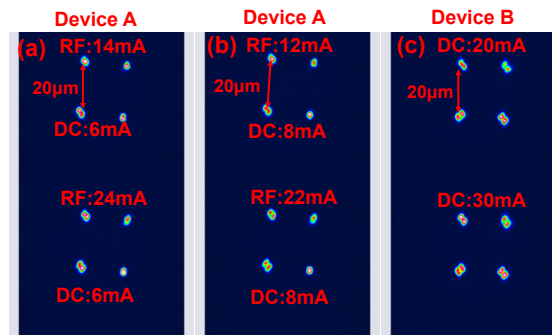
**Fig. 12.** Measured 2-D near-field patterns under two different total bias currents of 20 and 30 mA for (a) device A (dc electrode: 6 mA), (b) device A (dc electrode: 8 mA), and (c) device B ($W_z/W_o/d = 7/4/1.5$ μm).

(b), device A with its dual electrode design exhibits a wider maximum bandwidth (19 vs. 16 GHz) for a small W_o. This is because, in the device A structure, the required photon density for bandwidth enhancement is partially supplied by the injection of optical power leakage from neighboring VCSEL units, which may be too weak to be visible in our NFPs, as illustrated in 12, instead of only by current injection, as in the case for device B. This can minimize the device heating effect, which is usually the bandwidth limiting factor for small W_o VCSELs under high current injection. A similar phenomenon has been reported for bandwidth enhancement in edge-emitting lasers under external light injection [29]. As shown in Fig. 12, as expected, the superior dynamic performance of device A compared to device B leads to a much better quality of 32 Gbit/sec eye-opening (smaller jitter). Moreover, only device A can support error-free 32 Gbit/sec transmissions through 500-meter OM5 MMF, as shown in Fig. 13.
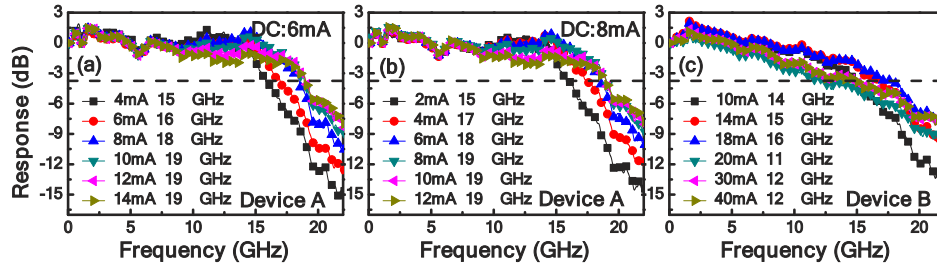
Fig. 13. Measured E-O frequency responses of (a) device A (dc electrode: 6 mA), (b) device A (dc electrode: 8 mA), and (c) device B under different bias currents ($W_z/W_o/d = 7/4/1.5\,\mu m$).
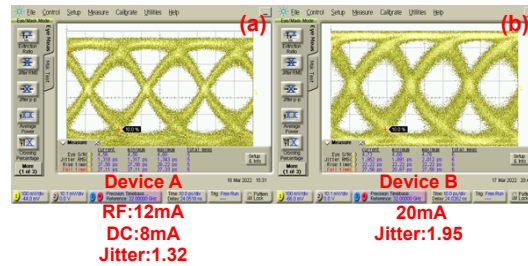
Fig. 14. Measured BTB 32 Gbit/sec transmission results using (a) device A and (b) device B ($W_z/W_o/d = 7/4/1.5\,\mu m$).
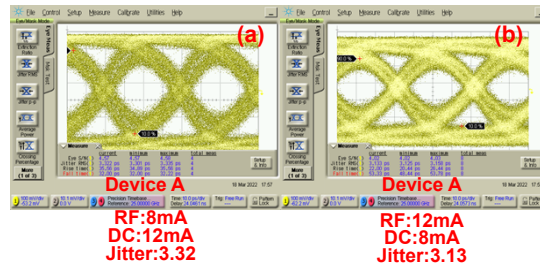
Fig. 15. Measured 32 Gbit/sec transmission results through a 500-meter OM5 fiber using device A with (a) (RF: 8 mA; dc: 12 mA) and (b) (RF: 12 mA; dc: 8 mA). ($W_z/W_o/d = 7/4/1.5\,\mu m$).

4. Conclusions

In this work, a novel design for the electrodes in a vertical-cavity surface-emitting laser (VCSELs) array is demonstrated. By separating the electrodes in a compact 2×2 VCSEL array into two parts, one for pure dc current injection and the other for large RF signal modulation, significant enhancement in the high-speed data transmission performance can be achieved. Compared with the single electrode reference array, the demonstrated array with its dual electrodes (dc + RF) design exhibits a more dampened electrical-optical (E-O) frequency response and a larger 3-dB E-O bandwidth (19 vs. 15 GHz) under the same total bias current amount (20 mA). These advantages lead to a much better quality of 32 Gbit/sec eye-opening than that of the reference device (jitter: 1.5 vs. 2.8 ps) and we can achieve error-free 32 Gbit/sec transmissions over a 500-m MMF under a moderate total bias current at 20 mA, which corresponds to a high near QSM optical output power (17 mW @ 20 mA) and Gaussian-like optical far-field pattern with a narrow divergence angle (FWHM: 10° at 20 mA). The superior dynamic and static performance of our dual electrode VCSEL array can be attributed to the weak optical coupling between neighboring VCSELs, which is induced by the non-uniform current injection through dual electrodes. Compared with the other approaches for increasing photon density inside the VCSEL cavity, such as shrinking of the aperture size or directly increasing the bias current, our demonstrated optical injection scheme can effectively minimize device heating induced bandwidth degradation.

Disclosures. The authors declare no conflicts of interest.

Data availability. Data underlying the results presented in this paper are not publicly available at this time but may be obtained from the authors upon reasonable request.

References

1. R. Safaisini, J. R. Joseph, and K. L. Lear, "Scalable High-CW-Power High-Speed 980-nm VCSEL Arrays," IEEE J. Quantum Electron. **46**(11), 1590–1596 (2010).
2. N. Haghighi, P. Moser, and J. A. Lott, "Power, Bandwidth, and Efficiency of Single VCSELs and Small VCSEL Arrays," IEEE J. Sel. Top. Quantum Electron. **25**(6), 1–15 (2019).
3. J.-L. Yen, X.-N. Chen, K.-L. Chi, J. Chen, and J.-W. Shi, "850 nm Vertical-Cavity Surface-Emitting Laser Arrays with Enhanced High-Speed Transmission Performance Over a Standard Multimode Fiber," J. Lightwave Technol. **35**(15), 3242–3249 (2017).
4. Z. Khan, Y.-H. Chang, T.-L. Pan, Y.-C. Zhao, Y.-Y. Huang, C.-H. Lee, J.-S. Chang, C.-Y. Liu, C.-Y. Lee, C.-Y. Fang, and J.-W. Shi, "High-Brightness, High-Speed, and Low-Noise VCSEL Arrays for Optical Wireless Communication," IEEE Access **10**, 2303–2317 (2022).
5. L. Zhang, Z. Wei, Z. Wang, Z. Geng, G. Wei, J. Cheng, H.-Y. Fu, and Y. Dong, "High-speed multi-user optical wireless communication between VCSEL-integrated electronic devices," Optics Communications **486**, 126774 (2021).
6. R.-F. Carson, M.-E. Warren, P. Dacha, T. Wilcox, J.-G. Maynard, D.-J. Abell, K.-J. Otis, and J.-A. Lott, "Progress in high-power, high-speed VCSEL arrays," Proc. SPIE **9766**, 97660B (2016).
7. M. E. Warren, D. Podva, P. Dacha, M. K. Block, C. J. Helms, J. Maynard, and R. F. Carson, "Low-divergence high-power VCSEL arrays for lidar application," Proc. SPIE **10552**, 14 (2018).
8. A. Liu, P. Wolf, J.- A. Lott, and D. Bimberg, "Vertical-cavity surface-emitting lasers for data communication and sensing," Photon. Res. **7**(2), 121–136 (2019).
9. P. Westbergh, J.-S. Gustavsson, and A. Larsson, "VCSEL Arrays for Multicore Fiber Interconnects with an Aggregate Capacity of 240 Gb/s," IEEE Photonics Technol. Lett. **27**(3), 296–299 (2015).
10. N. Ledentsov Jr., L. Chorchos, O. Y. Makarov, M.-B. Sanayeh, J.-R. Kropp, I.-E. Titkov, V.-A. Shchukin, V.-P. Kalosha, J.-P. Turkiewicz, and N. N. Ledentsov, "Advances in design and application of compact VCSEL arrays: from multicore fiber to optical wireless and beyond," Proc. SPIE **12020**, 10 (2022).
11. N. N. Ledentsov, Y. Makarov, V.-A. Shchukin, V.-P. Kalosha, N. Ledentsov Jr, L. Chorchos, M.-B. Sanayeh, and J.-P. Turkiewicz, "High Speed VCSEL Technology and Applications," J. Lightwave Technol. **40**(6), 1749–1763 (2022).
12. N. N. Ledentsov, V. A. Shchukin, V. P. Kalosha, N. N. Ledentsov Jr, J.-R. Kropp, M. Augustin, Ł. Chorchos, J. P. Turkiewicz, and J.-W. Shi, "Anti–waveguiding vertical–cavity surface–emitting laser at 850 nm: From concept to advances in high–speed data transmission," Opt. Express **26**(1), 445–453 (2018).

13. J.-W. Shi, C.-C. Chen, Y.-S. Wu, S.-H. Guol, and Y.-J. Yang, "High-Power and High-Speed Zn-Diffusion Single Fundamental-Mode Vertical-Cavity Surface-Emitting Lasers at 850 nm Wavelength," IEEE Photonics Technol. Lett. **20**(13), 1121–1123 (2008).

14. A. Haglund, J. S. Gustavsson, J. Vukusic, P. Modh, and A. Larsson, "Single fundamental mode output power exceeding 6 mW from VCSELs with a shallow surface relief," IEEE Photonics Technol. Lett. **16**(2), 368–370 (2004).

15. A. Pissis, U. Siegenthaler, D. Bonfrate, P. D. Kanungo, and E. Zibik, "940 nm High Power Single Transverse Mode Coherent VCSEL Array with Tunnel Junction Lithographic Aperture," *International Semiconductor Laser Conference (ISLC)*, 1–2 (2021).

16. A. Haglund, J. S. Gustavsson, P. Modh, and A. Larsson, "Dynamic mode stability analysis of surface relief VCSELs under strong RF modulation," IEEE Photonics Technol. Lett. **17**(8), 1602–1604 (2005).

17. J.-W. Shi, Z.-R. Wei, K.-L. Chi, J.-W. Jiang, J.-M. Wun, I.-C. Lu, J. (Jyehong) Chen, and Y.-J. Yang, "Single- Mode, High-Speed, and High-Power Vertical-Cavity Surface-Emitting Lasers at 850 nm for Short to Medium Reach (2 km) Optical Interconnects," J. Lightwave Technol. **31**(24), 4037–4044 (2013).

18. T. Gründl, P. Debernardi, M. Muller, C. Grasse, P. Ebert, K. Geiger, M. Ortsiefer, G. Bohm, R. Meyer, and M. C. Amann, "Record Single-Mode, High-Power VCSELs by Inhibition of Spatial Hole Burning," IEEE J. Sel. Top. Quantum Electron. **19**(4), 1700913 (2013).

19. S. T. M. Fryslie, M. P. T. Siriani, D. F. Siriani, M. T. Johnson, and K. D. Choquette, "37-GHz Modulation via Resonance Tuning in Single-Mode Coherent Vertical-Cavity Laser Arrays," IEEE Photonics Technol. Lett. **27**(4), 415–418 (2015).

20. X. Gu, M. Nakahama, A. Matsutani, M. Ahmed, A. Bakry, and F. Koyama, "850 nm transverse-coupled-cavity vertical-cavity surface-emitting laser with direct modulation bandwidth of over 30 GHz," Appl. Phys. Express **8**(8), 082702 (2015).

21. E. Heidari, H. Dalir, M. Ahmed, V.-J. Sorger, and R.-T. Chen, "Hexagonal transverse-coupled-cavity VCSEL redefining the high-speed lasers," Nanophotonics. **9**(16), 4743–4748 (2020).

22. J.-C. Shih, Z. Khan, Y.-H. Chang, and J.-W. Shi, "High-Brightness VCSEL Arrays with Inter-Mesa Waveguides for the Enhancement of Efficiency and High-Speed Data Transmission," IEEE J. Sel. Top. Quantum Electron. **28**(1), 1–11 (2022).

23. E. Lamothe, L.- D. A. Lundeberg, and E. Kapon, "Eigenmode analysis of phased-coupled VCSEL arrays using spatial coherence measurements," Opt. Lett. **36**(15), 2916–2918 (2011).

24. Intelligent Epitaxy Technology, Inc., 1250 E Collins Blvd., Richardson, TX 75081, http://intelliepi.com

25. H. Li, P. Wolf, P. Moser, G. Larisch, A. Mutig, J. A. Lott, and D. H. Bimberg, "Impact of the Quantum Well Gain-to-Cavity Etalon Wavelength Offset on the High Temperature Performance of High Bit Rate 980-nm VCSELs," IEEE J. Quantum Electron. **50**(8), 613–621 (2014).

26. R. Safaisini, E. Haglund, P. Westbergh, J.S. Gustavsson, and A. Larsson, "20 Gbit/s data transmission over 2 km multimode fibre using 850 nm mode filter VCSEL," Electron. Lett. **50**(1), 40–42 (2014).

27. K.-L. Chi, Y.-X. Shi, X.-N. Chen, Jason (Jyehong) Chen, Y.-J. Yang, J.-R Kropp, N. Ledentsov Jr, M. Agustin, N.N. Ledentsov, G. Stepniak, J. P. Turkiewicz, and J.-W. Shi, "Single-Mode 850 nm VCSELs for 54 Gbit/sec On-Off Keying Transmission Over 1 km Multi-Mode Fiber," IEEE Photonics Technol. Lett. **28**(12), 1367–1370 (2016).

28. D. M. Kuchta, J. Gamelin, J. D. Walker, J. Lin, K. Y. Lau, and J. S. Smith, "Relative intensity noise of vertical cavity surface emitting lasers," Appl. Phys. Lett. **62**(11), 1194–1196 (1993).

29. X. Jin and S. L. Chuang, "Microwave modulation of a quantum-well laser with and without external optical injection," IEEE Photonics Technol. Lett. **13**(7), 648–650 (2001).